Microchimica Acta (2021) 188:425
https://doi.org/10.1007/s00604-021-05092-6

ORIGINAL PAPER

Sensitive sandwich-type electrochemical SARS-CoV-2 nucleocapsid protein immunosensor

Ceren Karaman[1] · Bahar Bankoğlu Yola[2] · Onur Karaman[3] · Necip Atar[4] · İlknur Polat[5] · Mehmet Lütfi Yola[5]

Received: 30 September 2021 / Accepted: 7 November 2021

Abstract

A sensitive and fast sandwich-type electrochemical SARS-CoV-2 (COVID-19) nucleocapsid protein immunosensor was prepared based on bismuth tungstate/bismuth sulfide composite (Bi_2WO_6/Bi_2S_3) as electrode platform and graphitic carbon nitride sheet decorated with gold nanoparticles (Au NPs) and tungsten trioxide sphere composite (g-C_3N_4/Au/WO_3) as signal amplification. The electrostatic interactions between capture antibody and Bi_2WO_6/Bi_2S_3 led to immobilization of the capture nucleocapsid antibody. The detection antibody was then conjugated to g-C_3N_4/Au/WO_3 via the affinity of amino-gold. After physicochemically characterization via transmission electron microscopy (TEM), scanning electron microscopy (SEM), x-ray diffraction (XRD), and x-ray photoelectron spectroscopy (XPS), cyclic voltammetry (CV), differential pulse voltammetry (DPV), and electrochemical impedance spectroscopy (EIS) analysis were implemented to evaluate the electrochemical performance of the prepared immunosensor. The detection of SARS-CoV-2 nucleocapsid protein (SARS-CoV-2 NP) in a small saliva sample (100.0 µL) took just 30 min and yielded a detection limit (LOD) of 3.00 fg mL^{-1}, making it an effective tool for point-of-care COVID-19 testing.

Keywords COVID-19 · g-C_3N_4/Au/WO_3 · Bi_2WO_6/Bi_2S_3 · Electrochemistry · Voltammetry · Electrochemical impedance spectroscopy · Immunosensor

Introduction

The recent coronavirus disease (COVID-19), which the World Health Organization (WHO) has proclaimed as a pandemic, has a significant impact on not just health but also the economy [1–3]. Therefore, the WHO urged the international community to conduct widespread diagnostic testing in an effort to fight against the virus spread and reduce the number of cases that go undetected [4]. The tools for diagnostic are critical in determining early treatment and isolation decisions for affected people, preventing or halting the spread of infectious diseases. As a consequence, developing a highly-sensitive, precise, and prompt diagnostics tools can be vital in deciding what is best about whether or not to isolate affected individuals, thereby controlling the spread rate of this fatal virus [4–6]. The "gold standard" technique in detecting severe acute respiratory syndrome coronavirus 2 (SARS-CoV-2) that leads COVID-19 can be regarded as the reverse-transcription polymerase chain reaction (RT-PCR) [7]. Although PCR-based tests seem to be specifically tailored for SARS-CoV-2, many variables, including sample variances and viral RNA persistence in the nasal cavity/throat, impact their accuracy, resulting in false-negative/false-positive test findings [8–10]. Furthermore, radiological imaging techniques like computed tomography (CT) are considered to be one of the most effective ways to detect the COVID-19. However, owing to some constraints such as being available only at health facilities, difficulties in accessibility, and high cost, it is unlikely to be utilized for swift and large-scale testing [11, 12]. Therefore, the development

✉ Mehmet Lütfi Yola
mlutfi.yola@hku.edu.tr

1 Department of Electricity and Energy, Vocational School of Technical Sciences, Akdeniz University, Antalya, Turkey

2 Science and Technology Application and Research Laboratory, Iskenderun Technical University, Hatay, Turkey

3 Department of Medical Imaging Techniques, Vocational School of Health Services, Akdeniz University, Antalya, Turkey

4 Department of Chemical Engineering, Faculty of Engineering, Pamukkale University, Denizli, Turkey

5 Department of Nutrition and Dietetics, Faculty of Health Sciences, Hasan Kalyoncu University, Gaziantep, Turkey

Published online: 23 November 2021

of time-saving, extremely sensitive, and precise, cost-effective COVID-19 electroanalytical sensing technologies is essential and would have a substantial impact on the control of the pandemic [13].

There has recently been a drive to fabricate COVID-19 serological assays that identify immunological or viral proteins in the blood sample of infected people. Since proteins are homogenously distributed in the blood, serological specimens are more persistent than viral RNA and have fewer variations than nasopharyngeal or oropharyngeal viral RNA specimens, reducing the risk of false-negative test findings [14]. In a few publications, it has been established that lateral flow immunoassay (LFA) methods incorporating colorimetry/fluorescence approaches for targeting the IgG, IgM, or IgA immunoglobulins generated as a reaction to SARS-CoV-2 during the early stages of infection may accurately diagnose viral RNA [8, 15–21]. Moreover, the serological assays will aid in assessing a population's immunological response to spontaneous infection as well as vaccination [7]. Despite the fact that these devices are user-friendly and swift, they generally have low sensitivity and need at least two antibodies to detect. Therefore, electrochemical monitoring of SARS-CoV-2 antibodies has emerged as a viable approach to solve these limitations [7]. This technique has a high ability to distinguish tiny differences on the electrode surface from the recognition case, thereby allowing label-free detection without any need for a single antibody. Electrochemical immunosensors have significant features that are appropriate for today's needs, such as simplicity of use, cost and time effectiveness, portability, swiftness, and high sensitivity [13]. Previously, various electrochemical biosensors were employed to detect viral antigens from a variety of fatal viruses, including Hepatitis, Dengue, Rabies, and Zika [22–24]. Moreover, due to the current COVID-19 pandemic, biosensor research aimed at identifying and quantifying SARS-CoV-2 has emerged. However, interfacial contamination caused by biomolecule adsorption is one of the most serious challenges with electrochemical sensing technologies, limiting their practical applicability [25]. Therefore, the fabrication of an effictice immunosensor surface modified with suitable nanomaterials, which restricts non-specific adsorption of molecules without interacting with particular analyte detection, is one plausible option to this challenge.

Semiconductor nanocrystals were used for various applications such as energy [26], supercapacitor electrode material [27, 28], and catalysis [29]. Especially, bismuth-based semiconductors having specific morphology show desirable sensor catalytic performance [30, 31]. Among these semiconductors, bismuth sulfide (Bi_2S_3) belonging a tunable band gap (from 1.2 to 1.8 eV) demonstrates good stability, non-toxicity, and conductivity, providing superior electronic properties for sensor/biosensor applications. Nonetheless, owing to the easy photogenerated carrier recombination, its practical applications are limited. In order to eliminate this carrier recombination problem, the several methods such as the element dopping and the preparation of heterostructures can be utilized for improvement of catalytic activity. The layered Bi_2WO_6 has received a great deal of interest thanks to its stability and superior catalytic properties [32]. Its layered structure composes of the octahedral $(WO_4)^{2-}$ sheets and bismuth oxide $(Bi_2O_2)^{2+}$ layers, indicating easy charge transfer. This structure was formed by an intergrowth of WO_4^{2-} ions between $(Bi_2O_2)^{2+}$ layers [33]. Due to internal electric field, the recombination of charge carriers is reduced and sensor/biosensor's catalytic activity increases. In addition, its application areas can be expanded by dopping treatment [34] and the heterojunction construction [35]. In these methods, the coupling with two different semiconductor into heterojunctions is effective approach [36]. Thus, we prepared Bi_2WO_6/Bi_2S_3 as electrode platform in this study.

The preparation of g-C_3N_4 can be carried out by thermal pyrolysis of nitrogen-rich precursors such as melamine and urea [37]. Due to its excellent stability, low toxicity and conductivity, it has been utilized in electrochemical applications [38]. g-C_3N_4 with band gap of 2.7 eV and WO_3 with band gap of 2.8 eV can be made up of a Z-scheme heterojunction [39], providing the prevention of the electron–hole recombination. In addition, tungsten trioxide (WO_3) has superior electronic and chemical properties and biocompatibility [40]. A mediator such as AuNPs is generally needed for facilitating the electron transfer in Z-scheme heterojunction. Due to AuNPs' electrical conductivity and large specific surface area, the immobilization of antibodies also becomes easier [41]. Hence, g-C_3N_4/Au/WO_3 as signal amplification can separate electron–hole, providing the sensitivity of sensor performance.

Herein, in the light of all aforementioned points in mind, it was aimed to fabricate a novel electrochemical SARS-CoV-2 nucleocapsid protein immunosensor based on Bi_2WO_6/Bi_2S_3 and g-C_3N_4/Au/WO_3 for COVID-19 detection for the first time in literature. The fabricated immunosensor provides a number of benefits, including ease of use, speed, and selectivity. Moreover, a precise LOD of 3.00 fg mL^{-1} was acquired with high selectivity and no interference in saliva samples. Hence, the fabricated electrochemical SARS-CoV-2 nucleocapsid protein immunosensor presents a new perspective in the point-of-care COVID-19 testing.

Experimental section

Materials

SARS-CoV-2 NP, capture human monoclonal anti-SARS-CoV-2 nucleocapsid antibody (c-SARS-CoV-2-Ab_1), detection monoclonal anti-SARS-CoV-2 nucleocapsid antibody (d-SARS-CoV-2-Ab_2), MERS-CoV nucleocapsid protein (MERS-CoV NP), coronavirus nucleoprotein (SARS-CoV NP), influenza A antigen (H1N1), $Bi(NO_3)_3{\cdot}5H_2O$, $Na_2S{\cdot}9H_2O$, carbamide, $Na_2WO_4{\cdot}2H_2O$, melamine, sodium borohydride ($NaBH_4$), and chloroauric acid ($HAuCl_4$) were supplied from Sigma-Aldrich. Moreover, during the experiments, 0.1 mol.L^{-1} phosphate-buffered saline (PBS) solution with a pH value of 7.0 was employed as a supporting electrolyte and diluting buffer solution.

Apparatus for evaluation of nanomaterials

Surface morphological characteristics were explored by using a SEM (ZEISS EVO 50) SEM and a TEM (JEOL 2100). X-ray spectrum of nanostructrues was collected by a Rigaku X-ray diffractometer with Cu-K radiation ($\lambda = 0.150$ nm). The PHI 5000 Versa Probe spectrometer was used to perform the XPS survey. UV–Vis and Raman measurements were performed by Mettler Toledo and LabRam HR Raman Spectrometer, respectively. Electrochemical characterization techniques such as cyclic voltammetry, differential pulse voltammetry, and electrochemical empdance spectroscopy were also conducted via the Gamry Reference 600 workstation (Gamry, USA).

Preparation of Bi_2WO_6, Bi_2S_3, and Bi_2WO_6/Bi_2S_3

For preparation of Bi_2S_3 nanorods, the addition of $Bi(NO_3)_3{\cdot}5H_2O$ (1.90 g) into ethanol solution (30.0 mL) was firstly performed and stirred during 30 min. Then, $Na_2S{\cdot}9H_2O$ aqueous solution (0.1 g mL^{-1}) was prepared, stirred during 45 min and slowly added into $Bi(NO_3)_3{\cdot}5H_2O$ solution, providing the black suspension. After that, carbamide solution (0.1 g mL^{-1}) was transferred into the above solution and the suspension was subjected to 200 °C for 20 h in a Teflon steel autoclave. Bi_2S_3 nanorods were filtered, washed, and dried at 25.0 °C.

For preparation of Bi_2WO_6, the mixture of $Na_2WO_4{\cdot}2H_2O$ (3.0 mmol, 10.0 mL) and $Bi(NO_3)_3{\cdot}5H_2O$ (3.0 mmol, 10.0 mL) was prepared and strongly stirred during 20 min. Then, the mixture was subjected to 200 °C for 15 h in a Teflon steel autoclave. The resulting product as Bi_2WO_6 was filtered, washed, and dried at 60.0 °C.

To prepare Bi_2WO_6/Bi_2S_3 composite, Bi_2S_3 nanorods (10.0 mmol) and Bi_2WO_6 (10.0 mmol) were mixed at 1:1, v/v for 40 min. After that, Bi_2WO_6/Bi_2S_3 composite having heterojunction was collected, filtered, and dried at 40 °C.

Bi_2WO_6/Bi_2S_3 modified GCE (Bi_2WO_6/Bi_2S_3/GCE) as electrochemical sensor platform with c-SARS-CoV-2-Ab_1 and SARS-CoV-2 NP immobilizations

The glassy carbon electrode (GCE) was prepared as follows to be utilized in the further steps [42]: firstly, 0.1 µm and 0.05 µm alumina slurries were transferred on cleaning pads, respectively. Then, the GCE was polished with these alumina slurries for 20 min. Subsequently, the electrodes were rinsed with isopropyl alcohol and acetonitrile, respectively to remove the alumina remains at 25 °C. The electrode modifications with Bi_2WO_6, Bi_2S_3, and Bi_2WO_6/Bi_2S_3 suspensions (10.0 µL, 0.1 mg mL^{-1}) were performed by dropping these suspensions on the clean GCEs. After 20 min, the solvent removal was carried out by infrared heat lamp, providing Bi_2WO_6, Bi_2S_3, and Bi_2WO_6/Bi_2S_3 modified GCEs (Bi_2WO_6/GCE, Bi_2S_3/GCE, and Bi_2WO_6/Bi_2S_3/GCE). The c-SARS-CoV-2-Ab_1 immobilization on Bi_2WO_6/Bi_2S_3/GCE was performed by dropping of 20 µL c-SARS-CoV-2-Ab_1 dispersion (with a concentration of 20.0 µg.mL^{-1}) on Bi_2WO_6/Bi_2S_3/GCE via strong electrostatic interactions between amino group of c-SARS-CoV-2-Ab_1 and bismuth oxide $(Bi_2O_2)^{2+}$. The electrodes were maintained at 37.0 °C for 15 min (c-SARS-CoV-2-$Ab_1/Bi_2WO_6/Bi_2S_3$/GCE). Then, BSA (3.0% w/v) was incubated on c-SARS-CoV-2-$Ab_1/Bi_2WO_6/Bi_2S_3$/GCE at 37.0 °C over 15 min to eliminate the non-specific interactions (BSA/c-SARS-CoV-2-$Ab_1/Bi_2WO_6/Bi_2S_3$/GCE). Each of SARS-CoV-2 NP with different concentrations was incubated to BSA/c-SARS-CoV-2-$Ab_1/Bi_2WO_6/Bi_2S_3$/GCE for 15 min at 37.0 °C via specific protein-antibody interactions (SARS-CoV-2 NP/BSA/c-SARS-CoV-2-$Ab_1/Bi_2WO_6/Bi_2S_3$/GCE). Lastly, the whole electrode including SARS-CoV-2 NP and c-SARS-CoV-2-Ab_1 was interacted with 0.1 M PBS (pH 7.0) to take away non-interacting SARS-CoV-2 nucleocapsid proteins.

Preparation of g-C_3N_4, g-C_3N_4/WO_3, and g-C_3N_4/Au/WO_3

Firstly, g-C_3N_4 preparation was performed [43]. For this aim, the calcination of melamine (20.0 g) was conducted at 500 °C over 90 min. After the cooling treatment at 25 °C, the obtained yellow product was transferred into the combustion boat and the calcination treatment was performed at 480 °C for 120 min and after cooling, the white g-C_3N_4 was obtained.

For g-C_3N_4/WO_3 preparation [44], the mixture of g-C_3N_4 (0.25 g), $Na_2WO_4 \cdot 2H_2O$ (1.00 g), and ethanol (150.0 mL) was prepared under strong stirring. Afterward, the concentrated HCl (10.0 mL) was gently added into this mixture and the dispersion was calcined at 420 °C for 120 min, providing g-C_3N_4/WO_3 composite.

For g-C_3N_4/Au/WO_3 preparation, the mixture of g-C_3N_4/WO_3 (150.0 mg), $HAuCl_4$ (50.0 µL, 20.0 mM), and ultrapure water (50.0 mL) was prepared. After that, $NaBH_4$ (2.0 mL, 20.0 mM) was added into this dispersion under strong stirring and g-C_3N_4/Au/WO_3 was dried at 25 °C.

g-C_3N_4/Au/WO_3 signal amplification with d-SARS-CoV-2-Ab_2 conjugation

d-SARS-CoV-2-Ab_2 conjugation was performed by addition of detection antibody (20.0 µL, 20.0 µg mL^{-1}) into g-C_3N_4/Au/WO_3 (20.0 µL, 20.0 mg mL^{-1}) signal amplification via strong amino-gold affinity [45, 46]. After the vigorous stirring at 37.0 °C for 30 min, d-SARS-CoV-2-Ab_2/g-C_3N_4/Au/WO_3 was centrifugated at 5000 rpm for 30 min.

Electrochemical characterizations

The resulting SARS-CoV-2 nucleocapsid protein immunosensor was constructed by antibody-nucleocapsid protein interactions between d-SARS-CoV-2-Ab_2/g-C_3N_4/Au/WO_3 and SARS-CoV-2 NP/BSA/c-SARS-CoV-2-Ab_1/Bi_2WO_6/Bi_2S_3/GCE. By drop-casting method, 20.0 µL d-SARS-CoV-2-Ab_2/g-C_3N_4/Au/WO_3 dispersion (with a concentration of 20.0 mg mL^{-1}) was coated on electrode surface such as SARS-CoV-2 NP/BSA/c-SARS-CoV-2-Ab_1/Bi_2WO_6/Bi_2S_3/GCE, at a 30 min immunological response time. The final electrochemical immunosensor was tagged as g-C_3N_4/Au/WO_3/d-SARS-CoV-2-Ab_2/SARS-CoV-2 NP/BSA/c-SARS-CoV-2-Ab_1/Bi_2WO_6/Bi_2S_3/GCE and this electrochemical immunosensor was stored in 0.1 M PBS (pH 7.0, 3.0 mL) without pressure fluctuations at 25 °C. The electrochemical performance of the SARS-CoV-2 nucleocapsid protein immunosensor was monitored in 0.1 M PBS (pH 7.0, 2.0 mL) containing 1.0 mM H_2O_2 solution in the range of + 0.0/ + 0.4 V. Scheme 1 shows the preparation procedure of electrochemical SARS-CoV-2 immunosensor including the preparations of electrode platform and signal amplification.

Processing of samples

The saliva samples were acquired from five healthy individuals (See S. M. for a further description of sample processing).

Results and discussion

Fundamental of electrochemical SARS-CoV-2 NP immunosensor based on Bi_2WO_6/Bi_2S_3 and g-C_3N_4/Au/WO_3

Bi_2WO_6/Bi_2S_3 was employed as a sensor platform in immunosensor fabrication. Bi_2WO_6 with a layered structure comprises WO_4^{2-} ions' intergrowth between $(Bi_2O_2)^{2+}$ layers. Due to the layered structure, Bi6s and O2p levels create the dispersed valence band, providing the catalytic effect [47]. In addition, Bi_2WO_6 has important function as a framework to prepare Bi_2WO_6/Bi_2S_3 composite. Sodium sulfide as sulfur source can release S^{2-} ion to react with Bi_2WO_6 via ion change, providing Bi_2S_3 nanorods' dispersion [33]. In immunosensor construction, the efficient electrostatic interactions between amino group of c-SARS-CoV-2-Ab_1 and Bi_2WO_6/Bi_2S_3 composite also provided the strong capture antibody immobilization on electrode surface.

g-C_3N_4/Au/WO_3 composite was used as a signal amplification for electrochemical SARS-CoV-2 NP immunosensor. This composite composed a Z-scheme heterojunction [39], resulting in the decrease of the electron transfer. Hence, a mediator, which facilitated electron transfer, is necessary at the interface of heterojunction. AuNPs can be a candidate intermediate owing to their large specific surface area, the ability of the charge separation promotion, and the antibody's easy immobilization [48]. Hence, g-C_3N_4/Au/WO_3 composite both integrates substantial benefits and efficiently facilitates electron transport, thereby resulting in the development of a sensitive immunosensor.

Finally, H_2O_2 was utilized as a redox probe in this work due to its easy oxidation into O_2 and continuous monitoring. The related electrochemical reaction mechanism for H_2O_2 in potential range was also provided on Scheme 1 as $H_2O_2 \leftrightarrow O_2 + 2H^+ + 2e^-$ [49, 50].

Characterizations of Bi_2WO_6, Bi_2S_3, and Bi_2WO_6/Bi_2S_3

The morphological features of Bi_2WO_6, Bi_2S_3, and Bi_2WO_6/Bi_2S_3 composite were investigated on Fig. 1. The nanoflower and ultrathin nanosheet morphological structure of Bi_2WO_6 with about 2.5 µm diameter and 490–510 nm length were shown on Fig. 1A. Figure 1B shows pure Bi_2S_3 having a nanorod structure with width of 35–45 nm. In addition, the deposition of Bi_2S_3 nanorods with 120–140 nm lengths on Bi_2WO_6 nanoflower was shown on Fig. 1C. Finally, the elemental mapping of composite material (Fig. 1D) confirmed Bi_2WO_6/Bi_2S_3

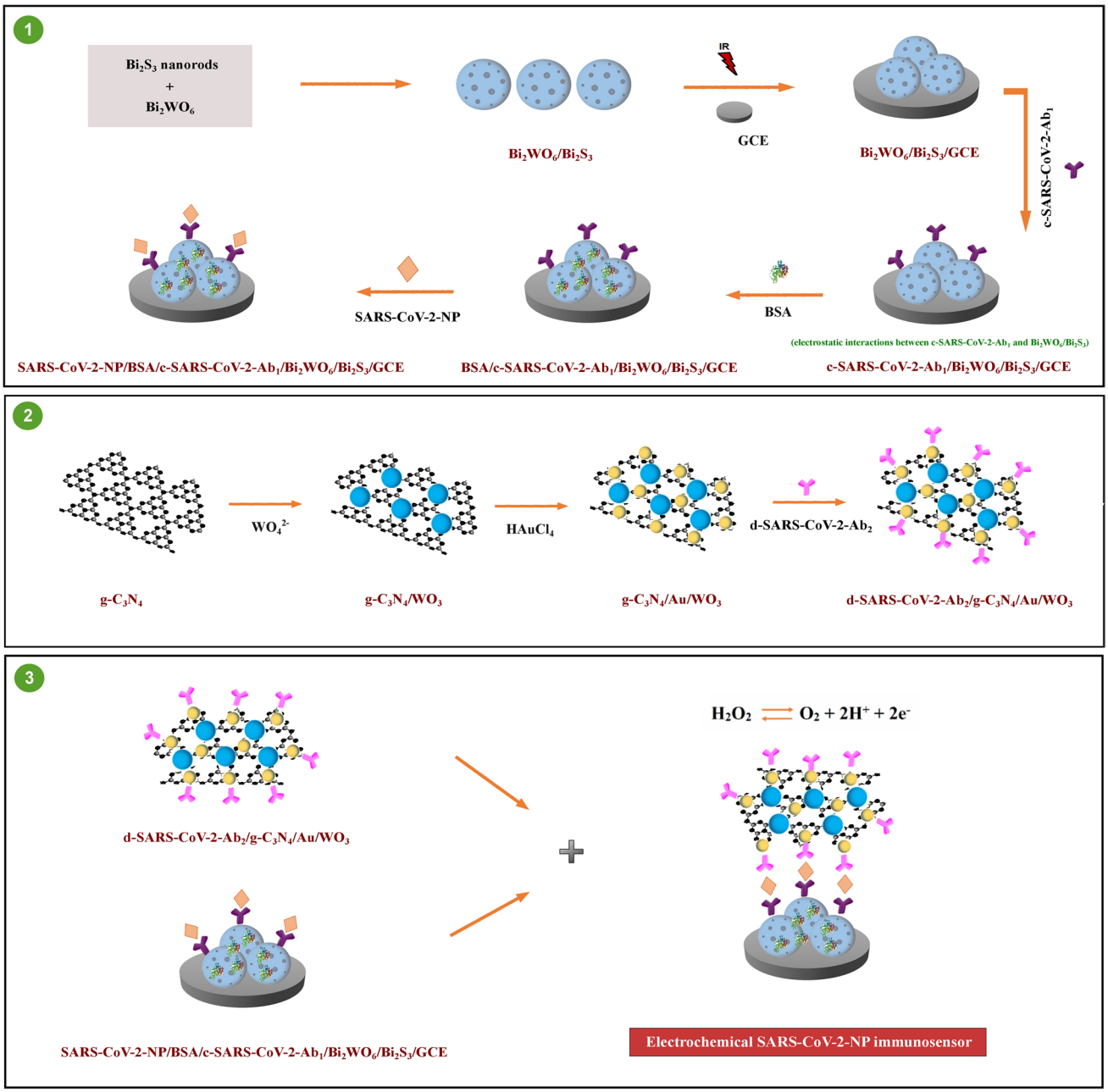

Scheme 1 Schematic illustration of the fabrication procedure of electrochemical SARS-CoV-2 immunosensor

formation in presence of Bi, W, and S. Secondly, XPS analysis was carried out to show the analysis patterns of Bi_2WO_6, Bi_2S_3, and Bi_2WO_6/Bi_2S_3 (Fig.S1AS1). According to Fig. S1A, Bi 4f7/2 peaks at 157.8 and 163.7 eV, Bi 4f5/2 peaks at 158.8 and 164.1 eV, and S 2p3/2 peak at 161.2 eV verified the presence of Bi^{3+} and S^{2-}, respectively. In addition, the peaks at 34.9 and 37.3 eV were ascribed to W 4f7/2 and W 4f5/2, respectively. Then, XRD patterns of Bi_2WO_6, Bi_2S_3, and Bi_2WO_6/Bi_2S_3 were demonstrated on Fig. S1B. The characteristic XRD peaks belonging to Bi_2WO_6 and Bi_2S_3 were attributed to the orthorhombic phases of Bi_2S_3 and Bi_2WO_6 [51, 52]. The same XRD peaks on the patterns of Bi_2WO_6 and Bi_2S_3 were observed on XRD pattern of Bi_2WO_6/Bi_2S_3 and it is concluded that Bi_2WO_6/Bi_2S_3 was prepared with a high purity.

According to Raman spectra (Fig. 2A), the obvious peaks such as the symmetric and asymmetric stretching peaks between W and O atoms on Bi_2WO_6 in 600–1000 cm^{-1} region were observed. Moreover, the band observed at 308 cm^{-1} was corresponded to O–WO– group's bending, whereas the bands detected

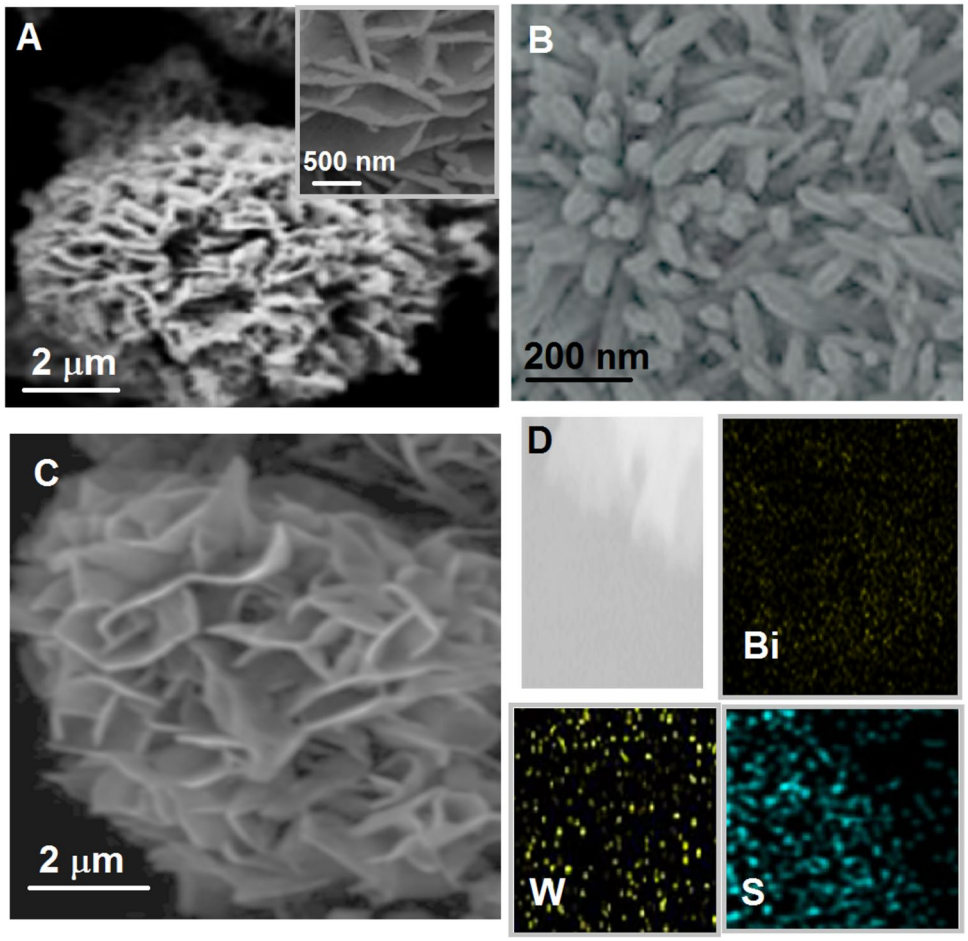

Fig. 1 SEM images of **A** Bi_2WO_6, **B** Bi_2S_3, and **C** Bi_2WO_6/Bi_2S_3; **D** elemental mapping of Bi_2WO_6/Bi_2S_3 composite

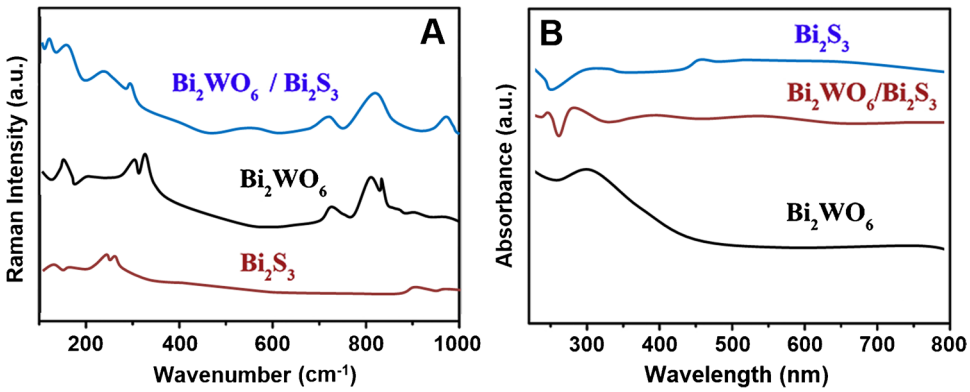

Fig. 2 Raman (**A**) and **B** UV–Vis spectra of Bi_2WO_6, Bi_2S_3, and Bi_2WO_6/Bi_2S_3

at 788 and 822 cm^{-1} were ascribed to asymmetrical and symmetrical modes of O–WO groups, respectively [53, 54]. The asymmetrical bridging mode relating to the tungstate chain was confirmed by the peak at 698 cm^{-1}. On Raman spectra of Bi_2WO_6/Bi_2S_3, the novel peaks at 101 and 229 cm^{-1} and the increased peak intensity at 254 cm^{-1} confirmed the presence of Bi_2S_3 on composite [55]. In addition, the specific bands attributing to Bi_2WO_6 were observed on Raman spectra of Bi_2WO_6/Bi_2S_3. Figure 2B demonstrates UV–Vis spectra of Bi_2WO_6, Bi_2S_3, and Bi_2WO_6/Bi_2S_3. The absorption band at about 440 nm showed the characteristic response of Bi_2WO_6 and the extended light absorption on the spectrum of Bi_2WO_6/Bi_2S_3 confirmed the synergistic effect between Bi_2WO_6 and Bi_2S_3 [56].

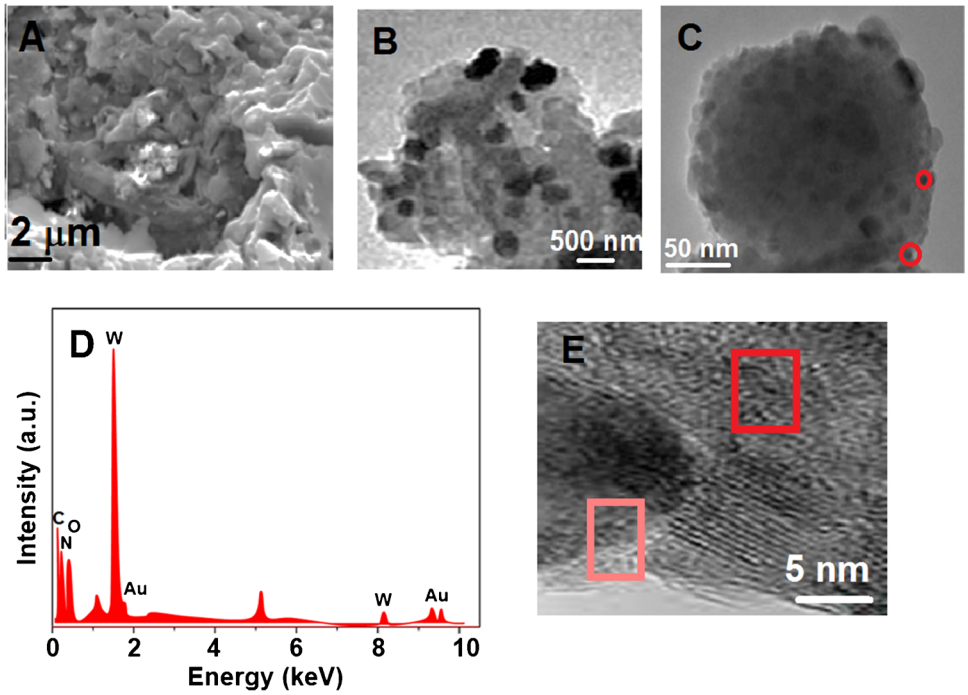

Fig. 3 **A** SEM image of g-C_3N_4, TEM images of **B** and **C** g-C_3N_4/Au/WO_3, **D** EDX image of g-C_3N_4/Au/WO_3, and **E** high-resolution TEM image of g-C_3N_4/Au/WO_3

Characterizations of g-C_3N_4, g-C_3N_4/WO_3, and g-C_3N_4/Au/WO_3

The crystalline structures and the surface morphologies of g-C_3N_4, g-C_3N_4/WO_3 and g-C_3N_4/Au/WO_3 were examined by TEM, SEM, XRD, and XPS techniques. The wrinkle structure of g-C_3N_4 was shown on Fig. 3A. According to Fig. 3B, it was revealed that WO_3 spheres with a diameter of 280–320 nm were uniformly decorated on g-C_3N_4 sheet, and AuNPs (red circle) with a small diameter placing between g-C_3N_4 and WO_3 were deposited on g-C_3N_4/WO_3 sheet (Fig. 3C). Furthermore, an EDX image of g-C3N4/Au/WO3 revealed the existence of C, N, O, W, and Au elements, noting that the g-C3N4/Au/WO3 was successfully fabricated (Fig. 3D). Finally, high-resolution TEM image (Fig. 3E) of g-C_3N_4/Au/WO_3 demonstrated the lattice spacing of Au NP (pink circle) and WO_3 (red circle), indicating 0.272 and 0.212 nm which were attributed to WO_3 (022) [57] and Au (200) [58].

The chemical states and the surface functionalities of g-C_3N_4/Au/WO_3 were examined through XPS analysis (Fig. S2). According to Fig. S2A of the survey spectra, the peaks belonging to C, N, O, W, and Au elements confirmed the successful preparation of g-C_3N_4/Au/WO_3 in harmony with Fig. 3D [59]. The high-resolution C1s XRD spectra of sample deconvoluted into two main peaks at 285.1 eV and 288.1 eV corresponded to C–C bond and N–C groups (Fig. S2B) [60]. Moreover, N1s spectra (Fig. S2C) were deconvoluted into three main N configurations with the peaks detected at 398.1, 399.4, and 401.1 eV attributing to C–N–C, –N = C–, and N–H, respectively [60]. The peak at 530.1 eV attributing to lattice oxygen and the peak at 532.2 eV corresponding to the chemisorbed oxygen species in WO_3 were demonstrated on Fig. S2D [61]. Fig.S2E relating to W 4f shows that W 4f7/2 and W 4f5/2 of W^{6+} were located at 35.1 and 37.9 eV, respectively [62]. Finally, the peaks at 84.1 and 88.1 eV were attributed to Au 4f7/2 and 4f5/2, respectively, indicating the existence of Au in composite material (Fig. S2F) [63].

The crystal structure of g-C_3N_4/Au/WO_3 composite was investigated by XRD (Fig. S3A). (002) crystal plane of g-C_3N_4 was confirmed by the peak at 27.62°. After the preparation of g-C_3N_4/Au composite, a new XRD peak at 38.31° was corresponded to Au NPs' (111) plane [64] and all peaks belonging to WO_3 were attributed to the monoclinic phase of WO_3 [65]. The observed peaks on XRD patterns of g-C_3N_4/WO_3 and g-C_3N_4/Au/WO_3 were similar to that of WO_3. In addition, the peak at 27.62° verified the presence of g-C_3N_4 and WO_3. Nonetheless, the specific peaks of Au NPs were not observed on XRD pattern of g-C_3N_4/Au/WO_3 composite, suggesting the low amount of Au NPs. UV–Vis spectra (Fig. S3B) were also recorded for g-C_3N_4, g-C_3N_4/WO_3, and g-C_3N_4/Au/WO_3. g-C_3N_4/Au/WO_3 composite having a wide absorption range effectively absorbs light, providing the increased catalytic response.

Evaluation of the electrochemical characteristics of sensor platform and signal amplification

Firstly, the electrochemical investigations for the prepared sensor platform were progressively performed by using CV

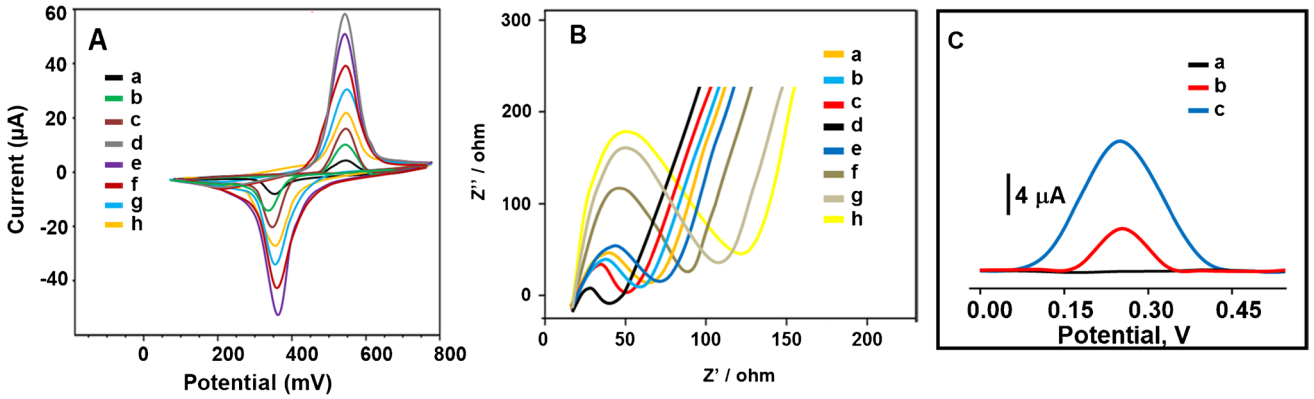

Fig. 4 **A** Cyclic voltammograms, **B** EIS reponses at (a) bare GCE, (b) Bi_2WO_6/GCE, (c) Bi_2S_3/GCE, (d) Bi_2WO_6/Bi_2S_3/GCE, (e) c-SARS-CoV-2-Ab_1/Bi_2WO_6/Bi_2S_3/GCE, (f) BSA/c-SARS-CoV-2-Ab_1/Bi_2WO_6/Bi_2S_3/GCE, (g) SARS-CoV-2 NP/BSA/c-SARS-CoV-2-Ab_1/Bi_2WO_6/Bi_2S_3/GCE, (h) the final immunosensor including c-SARS-CoV-2-Ab_1, SARS-CoV-2 NP, and d-SARS-CoV-2-Ab_2 (scan rate of 50 mV s^{-1}) in 1.0 mM $[Fe(CN)_6]^{3-}$ containing 0.1 M KCl, and **C** DPV responses of the proposed immunosensors incubated with 0.2000 pg mL^{-1} SARS-CoV-2 NP using g-C_3N_4/WO_3/d-SARS-CoV-2-Ab_2 (curve b) in presence of 1.0 mM H_2O_2, g-C_3N_4/Au/WO_3/d-SARS-CoV-2-Ab_2 (curve c) in presence of 1.0 mM H_2O_2 and in absence of target analyte (curve a)

and EIS methods in presence of 1.0 mM $[Fe(CN)_6]^{3-/4-}$ as redox pair. Firstly, the anodic and cathodic signals on bare GCE were observed at $Epa = 550$ mV and $Epc = 375$ mV, respectively, (curve a of Fig. 4A). Due to the high stability and catalytic activity of Bi_2WO_6/GCE in the presence of 1.0 mM $[Fe(CN)_6]^{3-/4-}$, more visible electrochemical signals were observed in contrast to bare glassy carbon electrode (curve b of Fig. 4A) [32]. Then, there was more electrochemical catalytic effect on the signals (curve c of Fig. 4A) by using Bi_2S_3/GCE, indicated the narrow band gap (1.3 eV) and the easy charge separation property [66]. Because Bi_2WO_6/Bi_2S_3 composites improved catalytic activity and the improved electron separation and transfer, the highest electrochemical responses in comparison with Bi_2S_3/GCE were obtained on Bi_2WO_6/Bi_2S_3/GCE (curve d of Fig. 4A). Electroactive surface areas of the prepared electrode surfaces were calculated as 0.173 ± 0.002 cm^2 for bare GCE, 0.319 ± 0.001 cm^2 for Bi_2WO_6/GCE, 0.647 ± 0.003 cm^2 for Bi_2S_3/GCE, and 1.113 ± 0.006 cm^2 for Bi_2WO_6/Bi_2S_3/GCE in the presence of 1.0 mM $[Fe(CN)_6]^{3-}$ solution by $i_p = 2.69 \times 10^5$ A $n^{3/2}$ $D^{1/2}$ C $v^{1/2}$, where i_p was current, C (mol cm^{-3}) was $[Fe(CN)_6]^{3-}$ concentration, v was scan rate (10–500 mV s^{-1}), and A was surface area (cm^2) ($n = 1$, $D = 7.6 \times 10^{-6}$ cm^2 s^{-1} for $[Fe(CN)_6]^{3-}$) [67]. Thus, Bi_2WO_6/Bi_2S_3 composite was chosen for future sensor platform.

As expected, the obvious electrochemical sensor signals decreased owing to c-SARS-CoV-2-Ab_1's blocking effect on electron transfer (curve e of Fig. 4A). After the immobilizations of BSA (curve f of Fig. 4A) and SARS-CoV-2 NP (curve g of Fig. 4A), respectively, we observed that the sensor signals gradually decreased. Thus, it is concluded that the immobilization treatments of BSA and SARS-CoV-2 NP on electrode surface were successfully carried out. Finally, when the resulting immunosensor was used (curve h of Fig. 4A), further decrease on sensor signals was observed because of more antibody-nucleocapsid protein interactions.

Secondly, EIS experiments were performed to prove CV results and according to Fig. 4B, the obtained charge transfer resistances were calculated as 75.0, 65.0, 55.0, 40.0, 85.0, 95.0, 125.0, and 140.0 Ω for bare GCE (curve a), Bi_2WO_6/GCE (curve b), Bi_2S_3/GCE (curve c), Bi_2WO_6/Bi_2S_3/GCE (curve d), c-SARS-CoV-2-Ab_1/Bi_2WO_6/Bi_2S_3/GCE (curve e), BSA/c-SARS-CoV-2-Ab_1/Bi_2WO_6/Bi_2S_3/GCE (curve f), SARS-CoV-2 NP/BSA/c-SARS-CoV-2-Ab_1/Bi_2WO_6/Bi_2S_3/GCE (curve g), and the final immunosensor (curve h), respectively. Hence, the preparation procedure of immunosensor was completed successfully based on CV and EIS results.

For electrochemical performance characterization (Fig. 4C) of the prepared signal amplification, several immunosensors using g-C_3N_4/WO_3/d-SARS-CoV-2-Ab_2 (curve b) and g-C_3N_4/Au/WO_3/d-SARS-CoV-2-Ab_2 (curve c) were developed by using 0.2000 pg mL^{-1} SARS-CoV-2 NP at the immune reaction time of 30 min and DPV signals were observed in 1.0 mM H_2O_2. As expected, the highest electrochemical performance was obtained by the immunosensor based on g-C_3N_4/Au/WO_3/d-SARS-CoV-2-Ab_2 in comparison with g-C_3N_4/WO_3/d-SARS-CoV-2-Ab_2. Because of the suppressing of electron transfer by g-C_3N_4/WO_3 composite, a mediator such as AuNPs was needed at the interface for improving of electron transfer in Z-scheme heterojunction [59]. In addition, the stable electrochemical signals were observed by g-C_3N_4/Au/WO_3/d-SARS-CoV-2-Ab_2 owing to the strong covalent immobilization between g-C_3N_4/Au/WO_3 and d-SARS-CoV-2-Ab_2. Curve a of Fig. 4C also demonstrated that there was no electrochemical signal in absence

of target analyte. To verify the specific interaction between antibody-nucleocapsid protein, SEM image (Fig. S4) of the resulting immunosensor indicating a spherical size and agglomeration was obtained, providing a successful immune reaction.

Optimization studies for electroanalytical characterizations

The effects of the solution pH, immune reaction time, H_2O_2, and g-C_3N_4/Au/WO_3/d-SARS-CoV-2-Ab_2 solution concentration were presented in detail (Fig. S5).

Linearity range

The obtained calibration equation by using SARS-CoV-2 NP concentrations and the observed electrochemical immunosensor signals was calculated as $y = 47.231x + 1.0666$, with a correlation coefficient of $R^2 = 0.9989$, where y and x represented the current (μA) and SARS-CoV-2 NP concentration (pg mL^{-1}), respectively (Fig. 5). The quantification limit (LOQ) and LOD were found to be 0.01 pg mL^{-1} and 3.00 fg mL^{-1}, respectively. Equations (1) and (2) were employed to calculate LOQ and LOD:

$$LOQ = 10.0\ \mathrm{S/m} \quad (1)$$

$$LOD = 3.3\ \mathrm{S/m} \quad (2)$$

In addition, Table 1 shows some comparison features between the developed sandwich-type electrochemical SARS-CoV-2 NP and the other new detection methods. Firstly, the sensitive SARS-CoV-2 NP detection (LOD:

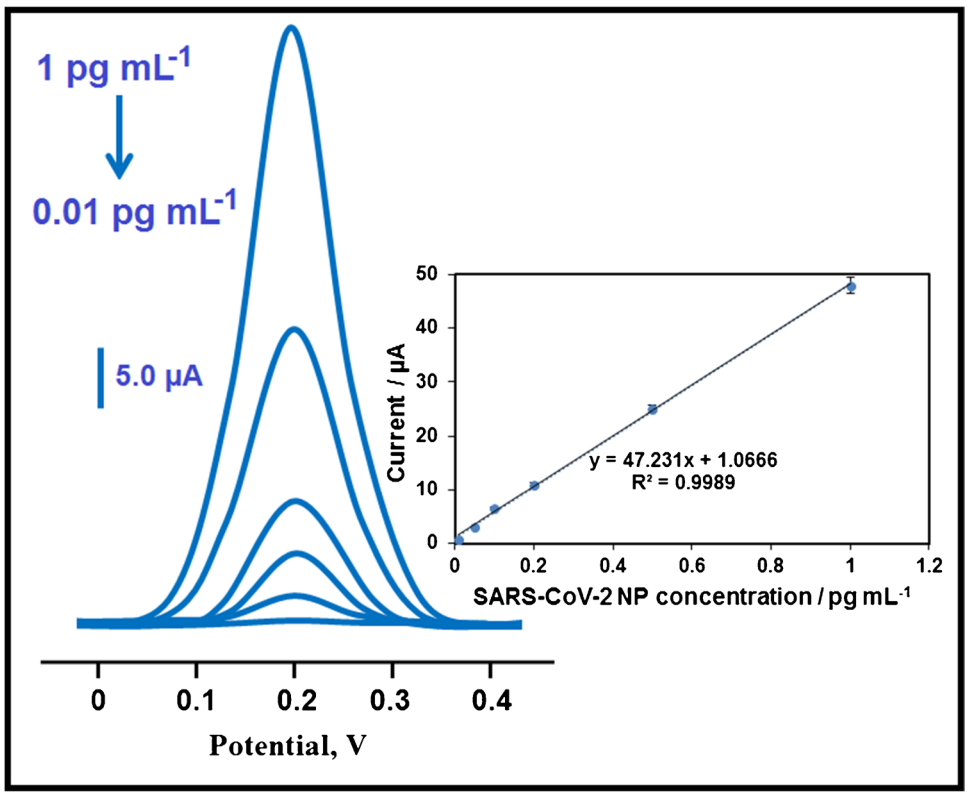

Fig. 5 Concentration effect (from 0.01 to 1.00 pg mL^{-1} SARS-CoV-2 NP) on immunosensor signals, Inset: calibration curve for electrochemical SARS-CoV-2 NP immunosensor (potential range is + 0.0/ + 0.4 V; Parameters are frequency of 100 Hz, pulse amplitude of 25 mV, and scan increment of 5 mV)

Table 1 The comparison of electrochemical SARS-CoV-2 NP immunosensor with the other novel techniques

Material/method	Linear range	LOD	Assay time	Ref
Microfluidic	0.0–10.0 ng mL^{-1}	50.0 pg mL^{-1}	2 min	[68]
Paper-based electrochemical	1.0–1000.0 ng mL^{-1}	1.0 ng mL^{-1}	30 min	[7]
Chemiluminescence	0.2–100.0 ng mL^{-1}	0.1 ng mL^{-1}	16 min	[69]
Electrochemical/Cu_2O nanocube	0.25 fg mL^{-1}–1.00 μg mL^{-1}	0.04 fg mL^{-1}	20 min	[70]
$Ni(OH)_2$ NPs	0.25 fg mL^{-1}–1.00 μg mL^{-1}	3.00 fg mL^{-1}	20 min	[71]
Electrochemical immunosensor	***0.01–1.00 pg mL^{-1}***	***3.00 fg mL^{-1}***	***30 min***	***This study***

3.00 fg mL^{-1}) was performed in 30 min of immunological response time. More importantly, COVID-19 detection with high selectivity can be successfully performed from saliva samples by this immunosensor. In addition, thanks to the developed electrochemical SARS-CoV-2 NP immunosensor, the time-consuming steps in immunosensor development can be eliminated in this study. The preparation steps of Bi_2WO_6/Bi_2S_3 electrode platform and g-C_3N_4/Au/WO_3 signal amplification comprised the minimal waste generation, indicating an immunosensor that is friendly to the environment and human health. As a result, the developed selective electrochemical SARS-CoV-2 NP immunosensor may offer a potential for early COVID-19 detection.

Recovery

The recovery experiments including saliva samples obtained from five healthy individuals were carried out by the portable electrochemical SARS-CoV-2 NP immunosensor. Table S1 indicates the close values to 100.00% confirming the preparation of high selective electrochemical SARS-CoV-2 NP immunosensor. Moreover, standard addition method was applied to saliva samples obtained from five healthy individuals and $y = 47.249x + 10.171$, with $R^2 = 0.9994$, was obtained as calibration equation. Thus, the close slope values between direct calibration (inset of Fig. 5) and standard addition methods again verified the high selective COVID-19 detection.

The validity of the sandwich-type electrochemical immunosensor was evaluated by using colorimetric method [72]. Table S2 indicates the comparison results, showing that no significant difference was observed between the prepared immunosensor and colorimetric method ($T_{calculated} > T_{tabulated}$, $p > 0.05$).

Selectivity, stability, reproducibility, and reusability

For selectivity measurement, the several electrochemical SARS-CoV-2 NP immunosensors were prepared by using different target dispersions such as (i) MERS-CoV NP + SARS-CoV NP + H1N1, (ii) SARS-CoV-2 NP + MERS-CoV NP, (iii) SARS-CoV-2 NP + SARS-CoV NP, (iv) SARS-CoV-2 NP + H1N1. Then, these electrochemical immunosensors were applied to 1.0 mM H_2O_2 solution. Figure 6A confirms that the prepared electrochemical immunosensor demonstrated the high selectivity towards SARS-CoV-2 nucleocapsid protein.

The stability test results of the constructed electrochemical SARS-CoV-2 NP immunosensor at 25.0 °C for seven weeks were depicted in Fig. 6B. It was pointed out that the immunosensor signals were about 98.73% of the original electrochemical signal, indicating strong immunosensor stability.

Finally, for reproducibility, 10 different electrochemical SARS-CoV-2 NP immunosensors were developed by the protocol which is explained in the "Electrochemical characterizations" section. The relative standard deviation (RSD) of 0.61 was calculated by using the observed 10 electrochemical signals, confirming the high reliability of immunosensor production procedure.

Reusability of prepared electrochemical SARS-CoV-2 NP immunosensor was tested in 1.0 mM H_2O_2 solution. One

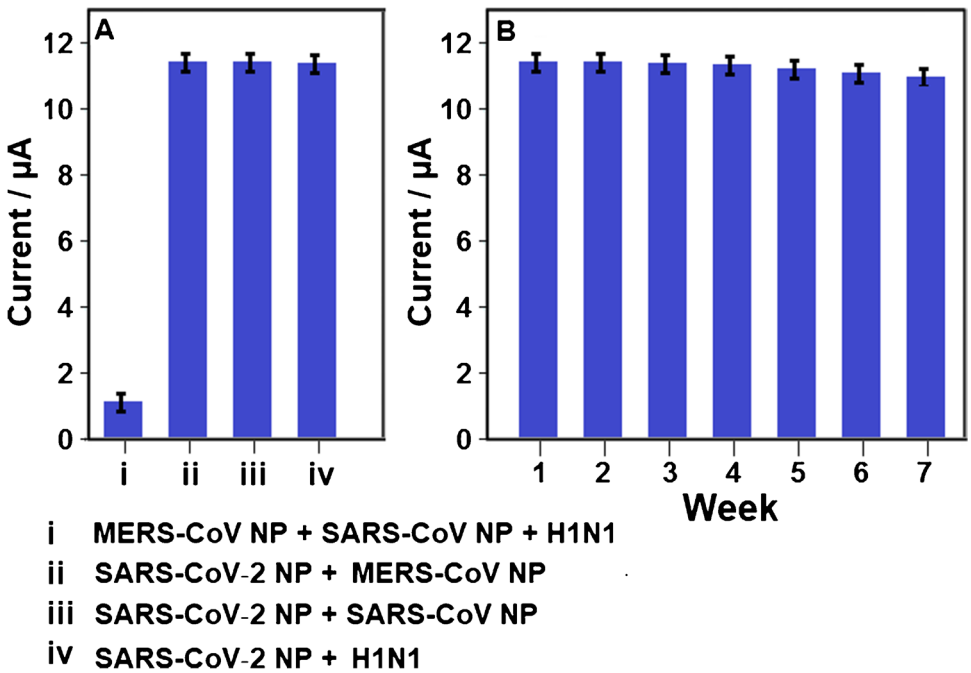

Fig. 6 **A** Immunosensor selective responses against the prepared solutions ($n = 6$): (i) 10.0 pg mL^{-1} MERS-CoV NP + 10.0 pg mL^{-1} SARS-CoV NP + 10.0 pg mL^{-1} H1N1, (ii) 0.2000 pg mL^{-1} SARS-CoV-2 NP + 10.0 pg mL^{-1} MERS-CoV NP, (iii) 0.2000 pg mL^{-1} SARS-CoV-2 NP + 10.0 pg mL^{-1} SARS-CoV NP, (iv) 0.2000 pg mL^{-1} SARS-CoV-2 NP + 10.0 pg mL^{-1} H1N1; **B** Stability test of electrochemical SARS-CoV-2 NP immunosensor including 0.2000 pg mL^{-1} SARS-CoV-2 NP ($n = 6$) at 25.0 °C

SARS-CoV-2 NP immunosensor was utilized at least 30 times and 0.89% of RSD was obtained for current signals, confirming high reusability of prepared electrochemical SARS-CoV-2 NP immunosensor in this study.

Precision and accuracy

The studies of same day (intra-day precision) and six consecutive days (inter-day precision) were carried out in presence of three concentrations (0.3000, 0.5000, and 0.7000 pg mL^{-1} SARS-CoV-2 NP) in linearity range (Table S3). The values of RSD for intra-day and inter-day precision were obtained as 0.070–0.098 and 0.035–0.098, respectively. Hence, low RSD verified high precision of prepared electrochemical SARS-CoV-2 NP immunosensor. Accuracy as Bias % was also tested and low Bias % (Table S3) suggested the high accuracy of electrochemical SARS-CoV-2 NP immunosensor.

Conclusions

COVID-19 pandemic has caused important damage to society. Until now, many kits for SARS-CoV-2 sensing have been developed. For first time, sensitive electrochemical SARS-CoV-2 nucleocapsid protein immunosensor based on Bi_2WO_6/Bi_2S_3 as electrode platform and g-C_3N_4/Au/WO_3 as signal amplification was presented in this work. This immunosensor was constructed by c-SARS-CoV-2-Ab_1 immobilization via strong electrostatic interaction and d-SARS-CoV-2-Ab_2 incubation via gold-amino affinity. Thus, the stable electrochemical signals were accomplished in terms of COVID-19 disease detection. In addition, the prepared electrochemical immunosensor had good ability in selective detection of SARS-CoV-2 nucleocapsid protein. In spite of these advantages, the presented detection protocol was a little time consuming in immunological response time (30 min), indicating that this analysis time is significant in terms of faster diagnosis. Furthermore, the prepared immunosensor based on Bi_2WO_6/Bi_2S_3 and g-C_3N_4/Au/WO_3 was reproducible and reusable biosensor and did not include in time-consuming steps such as sensor preparation. Finally, this developed immunosensor can be easily integrated into a commercial biosensor tool and used for the determination of the other viral diseases.

Supplementary Information The online version contains supplementary material available at https://doi.org/10.1007/s00604-021-05092-6.

Acknowledgements Mehmet Lütfi YOLA would like to express his gratitude to the Turkish Academy of Sciences for their precious support in respect to The Young Scientists Award Programme, TÜBA-GEBIP (2019).

Declarations

Conflict of interest The authors declare no competing interests.

References

1. Seo G, Lee G, Kim MJ, Baek SH, Choi M, Ku KB, Lee CS, Jun S, Park D, Kim HG, Kim SJ, Lee JO, Kim BT, Park EC, Kim SI (2020) Correction to rapid detection of COVID-19 causative virus (SARS-CoV-2) in human nasopharyngeal swab specimens using field-effect transistor-based biosensor. ACS Nano 14(9):12257–12258
2. Fauci AS, Lane HC, Redfield RR (2020) Covid-19 - navigating the uncharted. N Engl J Med 382(13):1268–1269
3. Nguyen TT, Le XTT, Nguyen NTT, Nguyen QN, Le HT, Pham QT, Ta NKT, Nguyen QT, Nguyen AN, Hoang MT, Pham HQ, Vu LG, Luong AM, Koh D, Nguyen TH, Tran BX, Latkin CA, Ho CSH, Ho RCM (2021) Psychosocial impacts of COVID-19 on healthcare workers during the nationwide partial lockdown in Vietnam in April 2020. Front Psychiatry. 12:562337
4. Morales-Narvaez E, Dincer C (2020) The impact of biosensing in a pandemic outbreak: COVID-19. Biosens Bioelectron. 163:112274
5. Pokhrel P, Hu C, Mao H (2020) Detecting the Coronavirus (COVID-19). ACS Sens 5(8):2283–2296
6. Udugama B, Kadhiresan P, Kozlowski HN, Malekjahani A, Osborne M, Li VYC, Chen H, Mubareka S, Gubbay JB, Chan WCW (2020) Diagnosing COVID-19: the disease and tools for detection. ACS Nano 14(4):3822–3835
7. Yakoh A, Pimpitak U, Rengpipat S, Hirankarn N, Chailapakul O, Chaiyo S (2021) Paper-based electrochemical biosensor for diagnosing COVID-19: detection of SARS-CoV-2 antibodies and antigen. Biosens Bioelectron. 176:112912
8. Zhang W, Du RH, Li B, Zheng XS, Yang XL, Hu B, Wang YY, Xiao GF, Yan B, Shi ZL, Zhou P (2020) Molecular and serological investigation of 2019-nCoV infected patients: implication of multiple shedding routes. Emerg Microbes Infect 9(1):386–389
9. Fang Y, Zhang H, Xie J, Lin M, Ying L, Pang P, Ji W (2020) Sensitivity of Chest CT for COVID-19: comparison to RT-PCR. Radiology 296(2):E115–E117
10. Wolfel R, Corman VM, Guggemos W, Seilmaier M, Zange S, Muller MA, Niemeyer D, Jones TC, Vollmar P, Rothe C, Hoelscher M, Bleicker T, Brunink S, Schneider J, Ehmann R, Zwirglmaier K, Drosten C, Wendtner C (2020) Virological assessment of hospitalized patients with COVID-2019. Nature 581(7809):465–469
11. Polat C, Karaman O, Karaman C, Korkmaz G, Balci MC, Kelek SE (2021) COVID-19 diagnosis from chest X-ray images using transfer learning: enhanced performance by debiasing dataloader. J Xray Sci Technol 29(1):19–36
12. Alhudhaif A, Polat K, Karaman O (2021) Determination of COVID-19 pneumonia based on generalized convolutional neural network model from chest X-ray images. Expert Syst Appl. 180:115141
13. Song Z, Ma Y, Chen M, Ambrosi A, Ding C, Luo X (2021) Electrochemical biosensor with enhanced antifouling capability for COVID-19 nucleic acid detection in complex biological media. Anal Chem 93(14):5963–5971
14. Xiao SY, Wu Y, Liu H (2020) Evolving status of the 2019 novel coronavirus infection: proposal of conventional serologic assays for disease diagnosis and infection monitoring. J Med Virol 92(5):464–467
15. Guo L, Ren L, Yang S, Xiao M, Chang YF, Dela Cruz CS, Wang Y, Wu C, Xiao Y, Zhang L, Han L, Dang S, Xu Y, Yang QW, Xu

SY, Zhu HD, Xu YC, Jin Q, Sharma L, Wang L, Wang J (2020) Profiling early humoral response to diagnose novel coronavirus disease (COVID-19). Clin Infect Dis 71(15):778–785
16. Liu W, Liu L, Kou G, Zheng Y, Ding Y, Ni W, Wang Q, Tan L, Wu W, Tang S, Xiong Z, Zheng S (2020) Evaluation of nucleocapsid and spike protein-based enzyme-linked immunosorbent assays for detecting antibodies against SARS-CoV-2. J Clin Microbiol 58(6):e00461-e420
17. Zhao J, Yuan Q, Wang H, Liu W, Liao X, Su Y, Wang X, Yuan J, Li T, Li J, Qian S, Hong C, Wang F, Liu Y, Wang Z, He Q, Li Z, He B, Zhang T, Fu Y, Ge S, Liu L, Zhang J, Xia N, Zhang Z (2020) Antibody responses to SARS-CoV-2 in patients with novel coronavirus disease 2019. Clin Infect Dis 71(16):2027–2034
18. Li Z, Yi Y, Luo X, Xiong N, Liu Y, Li S, Sun R, Wang Y, Hu B, Chen W, Zhang Y, Wang J, Huang B, Lin Y, Yang J, Cai W, Wang X, Cheng J, Chen Z, Sun K, Pan W, Zhan Z, Chen L, Ye F (2020) Development and clinical application of a rapid IgM-IgG combined antibody test for SARS-CoV-2 infection diagnosis. J Med Virol 92(9):1518–1524
19. Liu X, Wang J, Xu X, Liao G, Chen Y, Hu CH (2020) Patterns of IgG and IgM antibody response in COVID-19 patients. Emerg Microbes Infect 9(1):1269–1274
20. Chen Z, Zhang Z, Zhai X, Li Y, Lin L, Zhao H, Bian L, Li P, Yu L, Wu Y, Lin G (2020) Rapid and sensitive detection of anti-SARS-CoV-2 IgG, using lanthanide-doped nanoparticles-based lateral flow immunoassay. Anal Chem 92(10):7226–7231
21. Eissa S, Zourob M (2021) Development of a low-cost cotton-tipped electrochemical immunosensor for the detection of SARS-CoV-2. Anal Chem 93(3):1826–1833
22. Caygill RL, Blair GE, Millner PA (2010) A review on viral biosensors to detect human pathogens. Anal Chim Acta 681(1–2):8–15
23. Khan MZH, Hasan MR, Hossain SI, Ahommed MS, Daizy M (2020) Ultrasensitive detection of pathogenic viruses with electrochemical biosensor: state of the art. Biosens Bioelectron. 166:112431
24. Samson R, Navale GR, Dharne MS (2020) Biosensors: frontiers in rapid detection of COVID-19. 3 Biotech. 10(9):385
25. Wang G, Han R, Li Q, Han Y, Luo X (2020) Electrochemical biosensors capable of detecting biomarkers in human serum with unique long-term antifouling abilities based on designed multifunctional peptides. Anal Chem 92(10):7186–7193
26. Xu X, Liu Z, Zuo Z, Zhang M, Zhao Z, Shen Y, Zhou H, Chen Q, Yang Y, Wang M (2015) Hole selective NiO contact for efficient perovskite solar cells with carbon electrode. Nano Lett 15(4):2402–2408
27. Scholes GD (2011) Semiconductor nanostructures: two dimensions are brighter. Nat Mater 10(12):906–907
28. Yu Z, Tetard L, Zhai L, Thomas J (2015) Supercapacitor electrode materials: nanostructures from 0 to 3 dimensions. Energy & Environmental Science. 8:702–730
29. Meng X, Zhang Z (2017) Pd-doped Bi2MoO6 plasmonic photocatalysts with enhanced visible light photocatalytic performance. Appl Surf Sci 392:169–180
30. Li N, Sun YA, Wang FY, Huang CA, Fu CP, Zhang LN, Liu YQ, Ge SG, Yu JH (2021) Target dual-recycling-induced bipedal DNA walker and Bi2WO6/Bi2S3 cascade amplification strategy in photoelectrochemical biosensor for TP53 detection. Sensor Actuat B-Chem. 345:130386
31. Lv SZ, Zhang KY, Zeng YY, Tang DP (2018) Double photosystems-based "Z-scheme" photoelectrochemical sensing mode for ultrasensitive detection of disease biomarker accompanying three-dimensional DNA walker. Anal Chem 90(11):7086–7093
32. Li C, Chen G, Sun J, Rao J, Han Z, Hu Y, Zhou Y (2015) A novel mesoporous single-crystal-like Bi2WO6 with enhanced photocatalytic activity for pollutants degradation and oxygen production. ACS Appl Mater Interfaces 7(46):25716–25724
33. Yan L, Wang Y, Shen H, Zhang Y, Li J, Wang D (2017) Photocatalytic activity of Bi2WO6/Bi2S3 heterojunctions: the facilitation of exposed facets of Bi2WO6 substrate. Appl Surf Sci 393:496–503
34. Li WT, Huang WZ, Zhou H, Yin HY, Zheng YF, Song XC (2015) Synthesis and photoactivity enhancement of Ba doped Bi2WO6 photocatalyst. Mater Res Bull 64:432–437
35. Li M, Zhang L, Fan X, Zhou Y, Wu M, Shi J (2015) Highly selective CO 2 photoreduction to CO over gC 3 N 4/Bi 2 WO 6 composites under visible light. Journal of Materials Chemistry A 39(9):5189–5196
36. Zhang B, Tang Y, Wu X, Xie H, Zhao F, Zeng B (2021) Experimental and DFT studies of novel Z-scheme Bi-doped Bi2WO6/Bi2S3 pn/n homo/heterojunction and its application in cathodic photoelectrochemical immunosensing. Sensors and Actuators B: Chemical. 346:130455
37. Raizada P, Sudhaik A, Singh P, Hosseini-Bandegharaei A, Thakur P (2019) Converting type II AgBr/VO into ternary Z scheme photocatalyst via coupling with phosphorus doped g-C3N4 for enhanced photocatalytic activity. Separation and Purification Technology. 227:115692
38. Karaman C, Karaman O, Atar N, Yola ML (2021) Electrochemical immunosensor development based on core-shell high-crystalline graphitic carbon nitride@carbon dots and Cd0.5Zn0.5S/d-Ti3C2Tx MXene composite for heart-type fatty acid-binding protein detection. Microchimica Acta. 188(6): 182.
39. Meng J, Wang X, Liu Y, Ren M, Zhang X, Ding X, Guo Y, Yang Y (2021) Acid-induced molecule self-assembly synthesis of Z-scheme WO3/g-C3N4 heterojunctions for robust photocatalysis against phenolic pollutants. Chemical Engineering Journal. 403:126354
40. Xue JW, Yang L, Wang H, Yan T, Fan DW, Feng R, Du B, Wei Q, Ju HX (2019) Quench-type electrochemiluminescence immunosensor for detection of amyloid beta-protein based on resonance energy transfer from luminol@SnS2-Pd to Cu doped WO3 nanoparticles. Biosens Bioelectron 133:192–198
41. Zhang YX, Cao XY, Deng RX, Liu QY, Xia JF, Wang ZH (2019) DNA synergistic enzyme-mediated cascade reaction for homogeneous electrochemical bioassay. Biosensors & Bioelectronics. 142:111510
42. Yola ML, Atar N, Qureshi MS, Üstündağ Z, Solak AO (2012) Electrochemically grafted etodolac film on glassy carbon for Pb (II) determination. Sens Actuators, B Chem 171:1207–1215
43. Yola ML (2021) Sensitive sandwich-type voltammetric immunosensor for breast cancer biomarker HER2 detection based on gold nanoparticles decorated Cu-MOF and Cu2ZnSnS4 NPs/Pt/g-C3N4 composite. Mikrochim Acta 188(3):78
44. Jie X, Zeng D, Zhang J, Xu K, Wu J, Zhu B, Xie C (2015) Graphene-wrapped WO3 nanospheres with room-temperature NO2 sensing induced by interface charge transfer. Sens Actuators, B Chem 220:201–209
45. Glisic BD, Rychlewska U, Djuran MI (2012) Reactions and structural characterization of gold(III) complexes with amino acids, peptides and proteins. Dalton Trans 41(23):6887–6901
46. La Belle JT, Demirok UK, Patel DR, Cook CB (2011) Development of a novel single sensor multiplexed marker assay. Analyst 136(7):1496–1501
47. Zhou Y, Zhang Y, Lin M, Long J, Zhang Z, Lin H, Wu JC, Wang X (2015) Monolayered Bi2WO6 nanosheets mimicking heterojunction interface with open surfaces for photocatalysis. Nat Commun 6:8340
48. Mahato K, Purohit B, Bhardwaj K, Jaiswal A, Chandra P (2019) Novel electrochemical biosensor for serotonin detection based on gold nanorattles decorated reduced graphene oxide in biological fluids and in vitro model. Biosens Bioelectron. 142:111502
49. Yola ML, Atar N (2020) Amperometric galectin-3 immunosensor-based gold nanoparticle-functionalized graphitic carbon nitride

nanosheets and core-shell Ti-MOF@COFs composites. Nanoscale 12(38):19824–19832
50. Medetalibeyoglu H, Beytur M, Akyıldırım O, Atar N, Yola ML (2020) Validated electrochemical immunosensor for ultra-sensitive procalcitonin detection: carbon electrode modified with gold nanoparticles functionalized sulfur doped MXene as sensor platform and carboxylated graphitic carbon nitride as signal amplification. Sensors and Actuators B: Chemical. 319:128195
51. Wang H, Jian Y, Kong Q, Liu H, Lan F, Liang L, Ge S, Yu J (2018) Ultrasensitive electrochemical paper-based biosensor for microRNA via strand displacement reaction and metal-organic frameworks. Sens Actuators, B Chem 257:561–569
52. Chen J, Luo Z, Sun C, Huang Z, Zhou C, Yin S, Duan Y, Li Y (2019) Research progress of DNA walker and its recent applications in biosensor. TrAC Trends in Analytical Chemistry 120:115626
53. Li W, Ding X, Wu H, Yang H (2018) In-situ hydrothermal synthesis of TiO2/Bi2WO6 heterojunction with enhanced photocatalytic activity. Mater Lett 227:272–275
54. Tang QY, Chen WF, Lv YR, Yang SY, Xu YH (2020) Z-scheme hierarchical Cu2S/Bi2WO6 composites for improved photocatalytic activity of glyphosate degradation under visible light irradiation. Separation and Purification Technology. 236:116243
55. Zhang P, Cui Y, Yao Y, Wei W, Sun Y, Zhang K, Gao Y (2021) "Bi–O" vacancy-pairs induced photochromic behavior in Bi2WO6 ultrathin nanosheets. Solar Energy Materials and Solar Cells. 223:110988
56. Li N, Sun Y, Wang F, Huang C, Fu C, Zhang L, Liu Y, Ge S, Yu J (2021) Target dual-recycling-induced bipedal DNA walker and Bi2WO6/Bi2S3 cascade amplification strategy in photoelectrochemical biosensor for TP53 detection. Sensors and Actuators B: Chemical. 345:130386
57. Batool S, Idrees M, Javed MS, Saleem M, Kong J (2020) Engaging tailored capacity of layered WS2 via sulphur bonding coupled with polyetherimide (WS2@NC) nanocomposite for high power and improved lithium-ion storage. Materials Chemistry and Physics. 246:122832
58. Hsueh TJ, Wu SS (2021) Highly sensitive Co3O4 nanoparticles/MEMS NO2 gas sensor with the adsorption of the Au nanoparticles. Sensors and Actuators B: Chemical. 329:129201
59. Pei F, Feng S, Wu Y, Lv X, Wang H, Chen SM, Hao Q, Cao Y, Lei W, Tong Z (2021) Label-free photoelectrochemical immunosensor for aflatoxin B1 detection based on the Z-scheme heterojunction of g-C3N4/Au/WO3. Biosens Bioelectron. 189:113373
60. Karaman C, Karaman O, Atar N, Yola ML (2021) Sustainable electrode material for high-energy supercapacitor: biomass-derived graphene-like porous carbon with three-dimensional hierarchically ordered ion highways. Phys Chem Chem Phys 23(22):12807–12821
61. Lei J, Liu H, Yuan C, Chen Q, Liu JA, Wen F, Jiang X, Deng W, Cui X, Duan T, Zhu W (2021) Enhanced photoreduction of U (VI) on WO3 nanosheets by oxygen defect engineering. Chemical Engineering Journal. 416:129164
62. Liu X, Jin A, Jia Y, Xia T, Deng C, Zhu M, Chen C, Chen X (2017) Synergy of adsorption and visible-light photocatalytic degradation of methylene blue by a bifunctional Z-scheme heterojunction of WO3/g-C3N4. Appl Surf Sci 405:359–371
63. Zhao W, Dong Q, Sun C, Xia D, Huang H, Yang G, Wang G, Leung DY (2021) A novel Au/g-C3N4 nanosheets/CeO2 hollow nanospheres plasmonic heterojunction photocatalysts for the photocatalytic reduction of hexavalent chromium and oxidation of oxytetracycline hydrochloride. Chemical Engineering Journal. 409:128185
64. Chen L, Zeng X, Si P, Chen Y, Chi Y, Kim DH, Chen G (2014) Gold nanoparticle-graphite-like C3N4 nanosheet nanohybrids used for electrochemiluminescent immunosensor. 86: 4188–4195.
65. Yoon M, Oh Y, Hong S, Lee JS, Boppella R, Kim SH, Mota FM, Kim SO, Kim DH (2017) Synergistically enhanced photocatalytic activity of graphitic carbon nitride and WO3 nanohybrids mediated by photo-Fenton reaction and H2O2. Appl Catal B 206:263–270
66. Sarkar A, Ghosh AB, Saha N, Dutta AK, Srivastava DN, Paul P, Adhikary B (2015) Enhanced photocatalytic activity of Eu-doped Bi 2 S 3 nanoflowers for degradation of organic pollutants under visible light illumination. Catal Sci Technol 5(8):4055–4063
67. Yola ML (2021) Sensitive sandwich-type voltammetric immunosensor for breast cancer biomarker HER2 detection based on gold nanoparticles decorated Cu-MOF and Cu2ZnSnS4 NPs/Pt/g-C3N4 composite. Microchim Acta 188(3):78
68. Li J, Lillehoj PB (2021) Microfluidic magneto immunosensor for rapid, high sensitivity measurements of SARS-CoV-2 nucleocapsid protein in serum. ACS Sens 6(3):1270–1278
69. Liu D, Ju C, Han C, Shi R, Chen X, Duan D, Yan J, Yan X (2020) Nanozyme chemiluminescence paper test for rapid and sensitive detection of SARS-CoV-2 antigen. Biosens Bioelectron. 173:112817
70. Rahmati Z, Roushani M, Hosseini H, Choobin H (2021) Electrochemical immunosensor with Cu2O nanocube coating for detection of SARS-CoV-2 spike protein. Mikrochim Acta 188(3):105
71. Rahmati Z, Roushani M, Hosseini H, Choobin H (2021) An electrochemical immunosensor using SARS-CoV-2 spike protein-nickel hydroxide nanoparticles bio-conjugate modified SPCE for ultrasensitive detection of SARS-CoV-2 antibodies. Microchem J. 170:106718
72. Karakus E, Erdemir E, Demirbilek N, Liv L (2021) Colorimetric and electrochemical detection of SARS-CoV-2 spike antigen with a gold nanoparticle-based biosensor. Analytica Chimica Acta. 1182:338939